International Journal of Mechanical Sciences 202–203 (2021) 106534

Contents lists available at ScienceDirect

International Journal of Mechanical Sciences

journal homepage: www.elsevier.com/locate/ijmecsci

Effect of metal additive manufacturing residual stress on post-process machining-induced stress and distortion

Sumair Sunny[a], Ritin Mathews[a], Glenn Gleason[a], Arif Malik[a,*], Jeremiah Halley[b]

[a] Department of Mechanical Engineering, The University of Texas at Dallas, Richardson, TX 75080, USA
[b] Tech Manufacturing, LLC, 45 Cooperative Way, Wright City, Missouri, 63390 USA

ARTICLE INFO

Keywords:
Additive manufacturing
Directed energy deposition
Iterative stress reconstruction
High-speed machining
Residual stress
Distortion

ABSTRACT

This work represents the first investigation into the influence of residual stress (RS) from powder-based metal additive manufacturing (AM) on the post-process machining-induced stress and distortion for thin-walled components. Machined part distortion and surface residual stress pose major challenges in several industries, including for aerospace applications involving monolithic structures. However, the influence of initial RS in the bulk material on high-speed machining-induced stress and distortion is still not well understood. This is particularly true for more recent hybrid (additive and subtractive) manufactured components in which significant tensile and compressive RS develops from the rapid thermal cycles during the AM build. It is hypothesized in this work that, even for a simple thin-walled structure, the initial RS in the AM bulk material significantly influences the RS and distortion induced by high-speed machining. It is further hypothesized that the degree of influence of the initial RS on machining-induced RS and distortion varies significantly according to the specific tool path, even for the same net material removal. To test these hypotheses, a numerical modeling approach is presented considering a thin-walled directed energy deposition (DED) structure subjected to high-speed end-milling. A compatible RS field for the DED build is established using an iterative reconstruction algorithm based on limited neutron diffraction measurements, and the full reconstructed RS field is then imposed as an initial state in the end-milling simulation that follows. To assess the influence of the initial DED RS on the machining-induced stress and distortion, as well as to examine how this influence varies with machining strategy, two different tool paths are considered for the same net material removal, both with and without considering RS inherent to the DED build. The findings reveal significant influence of the DED RS on the high-speed machining-induced distortion and RS, and further, this influence is seen to vary greatly with the machining strategy. Normalized root-mean-square differences (NRMSD) of up to 25% and 29%, respectively, are observed in the machining-induced RS for the two different tool paths when DED inherent RS is considered. Likewise, maximum NRMSD of up to 44% and 40% are revealed in the post-machining distortion for the two respective machining strategies when DED RS is included. In addition, variations observed in the stress triaxiality computed during machining suggests that inclusion of the DED RS influences the localized response of the material near the tool-workpiece interface. The technical approach demonstrated can be extended beyond hybrid manufacturing to generate important scientific insights regarding distortion and machining-induced stress for conventionally manufactured monolithic components in the aerospace and other performance-critical industries.

1. Introduction

Almost all commercial, precision-machined monolithic components for specialty applications are feature-rich, and contain numerous holes, channels, slots, protrusions, etc., as well as thin-walled sections. The manufacture of such components is typical in the aerospace industry [1,2], wherein machined monolithic components are expected to allow for automated and seamless assembly. While corrective measures for violation of high-tolerance requirements are prohibitive in terms of both cost and re-work time, part distortion during machining nonetheless continues to be problematic, particularly as part tolerances become increasingly tighter. Such distortion or "warpage" may arise from a combination of factors including (1) initial residual stress (RS) in the bulk material [3–5], (2) excessive thermal expansion in the tool and/or workpiece [6,7], (3) machining parameters [8], (4) tool wear [9,10], (5) improper clamping of the workpiece [11,12], and (6) dynamic instability or chatter [13]. Although many of the aforementioned factors have been studied extensively in the literature, the influence of initial RS in the bulk material on high-speed machining-induced stress and distortion has not been widely examined, particularly in relation to emerging hy-

* Corresponding author.
E-mail address: Arif.Malik@utdallas.edu (A. Malik).

https://doi.org/10.1016/j.ijmecsci.2021.106534
Received 17 March 2021; Received in revised form 12 May 2021; Accepted 12 May 2021
Available online 20 May 2021

brid manufactured components. Historically, the influence of initial RS has received relatively little attention because other factors have been deemed more significant. However, as machined feature tolerances approach 1 μm on conventional wrought materials with size on the order of 1 m, and as additive manufacturing (AM) is increasingly being considered for smaller, less critical or highly complex geometries, the need to investigate the influence of initial RS becomes more evident. How an AM metal part warps and moves due to RS still presents a major challenge today. According to GE Additive, distortion, including after machining, remains one of the greatest challenges; as a default practice, production and prototype AM parts are therefore stress relieved [14], and in certain cases, AM parts are oversized to meet post-machining tolerances. In recent years, a limited number of studies have been published to reveal some influence of initial RS on machining-induced RS and distortion in thin-walled monolithic components, mainly related to the machining of conventional wrought aluminum stock (e.g., rolled and stress-relieved plate). For instance, Ma et al. [15] used the slitting technique [16] to characterize the bulk initial RS in 415 mm × 325 mm × 50 mm samples cut from 7050-T7451 rolled aluminum plate, and noted from simulations that when thin-walled monolithic components were machined from the parent plate, substantial alternating tensile and compressive RS could be observed for stress components in the longitudinal (rolling) direction and the long-transverse (plate width) direction as function of the plate thickness direction. The redistribution of stress that occurs during machining has been found to result in distortions that exceed specified tolerances [17], posing a major cause for concern for the aerospace industry (among others) in which such components are frequently used [18,19]. Chatelain et al. [3] attempted to examine the influence of initial RS on machining-induced stress and distortion by performing neutron diffraction (ND) measurements on aluminum alloy 7475-T7351 specimens before and after machining. One set of specimens obtained from the rolled plate was subjected to some (unspecified) stress relief, which resulted in a RS difference of up to 18 MPa compared to non-stress-relieved specimens from the same plate. From post-machining ND and coordinate measuring machine (CMM) data, it was suggested that the different initial RS states led to variations in the machining-induced stress and distortion; however, there was no mention of how the unspecified stress relief may have changed the microstructure (and mechanical properties), nor were there any details regarding the crystallographic plane along which ND measurements were performed. These factors can significantly influence the interpretation of ND data from which RS is determined. In another study, Third Wave Systems reported a numerical analysis performed on aluminum alloy 7050-T7451 rolled plate based on machining process data supplied by the Aviation Development Directorate [20]. Objectives of the study were to: (1) compute the distortion that arises as a result of machining-induced RS, (2) examine the machined part distortion due to the initial bulk RS, and (3) optimize the tool path to minimize distortion. The initial bulk RS along the longitudinal and long-transverse directions within the 304.8 mm × 304.8 mm × 63.5 mm plate was measured via the slitting method, and the RS magnitudes through the depth (plate thickness) exhibited a symmetric stress profile characteristic of rolling that varied between ±20 MPa. When assessing part distortion due to the initial RS, the latter was simply mapped to the finished part geometry, thereby limiting an understanding of the extent to which the machining-induced RS and distortion are coupled to the initial RS field. It should also be noted that only two components of initial RS were mapped, and details regarding the four remaining independent stress components in the wrought plate were not addressed.

On the basis of the foregoing discussion, two hypotheses are investigated in the demonstrated work, which considers a directed energy deposition (DED) fabricated thin-walled part subjected to high-speed machining: (i) it is first hypothesized that, even for a simple thin-walled structure, the initial RS in the bulk material significantly influences the machining-induced RS and distortion, and (ii) it is further hypothesized that the degree of influence of initial RS on the machining-induced RS and distortion varies significantly according to the specific tool path, even for the same net material removal.

A comprehensive new understanding into how RS in the bulk material affects machining-induced RS and part distortion will facilitate improved tool path planning, thus enabling manufacturers to deliver components with increasingly tighter tolerances, and with reduced internal rejection rates. Such knowledge can be of paramount importance to the emerging field of hybrid additive manufacturing, which combines additive and subtracting processes to exploit design flexibility and/or achieve enhanced part functionality [21]. A majority of commercially available hybrid-AM machines employ DED technology, wherein rapid thermal cycles can give rise to considerable residual stress and part distortion/warpage [22,23]. This serves as motivation for employing a DED initial RS field to test the two aforementioned hypotheses, in effort to learn how much of a difference (if any) arises in the machining-induced stress and part distortion due to differences in the tool path, and the extent to which the DED RS consideration affects this observation. Accordingly, Section 2 of this paper discusses the reconstruction of a DED RS field for a thin-walled Inconel 625 structure based on spatially-limited ND data for the component. Once a compatible RS field is reconstructed, it is subsequently imposed as an initial state in a high-speed machining (end milling) simulation that features two very different tool paths, as described in Section 3. In addition, Section 3 comprehensively discusses the material constitutive modeling as well as competing damage models implemented within the high-speed machining simulation. A comparison of the stress and distortion resulting from the two tool paths, illustrating the respective influences of DED RS, is presented in Section 4. While this work considers RS and distortion for a 7 mm wall, intuitively these issues can be inferred to be more problematic for higher aspect ratio thin-walled structures (e.g. 1 to 2 mm) widely found in industry, although the exact causes of final distortion remains to be well understood. The examination of the in-situ stress triaxiality, which gives insight into how inclusion of DED RS can affect the material removal during the machining operation, is also given in Section 4. Finally, key findings deduced from studying the effects of initial RS on high-speed machining-induced RS and distortion are summarized in Section 5.

2. Reconstruction of directed energy deposition residual stress field for a thin-walled component

In this work, a DED build described by [24,25] is adopted to obtain a thin-walled structure with as-built initial RS field, however, it should be noted that the demonstrated work is extensible to thin-walled structures made by other manufacturing techniques as well.

2.1. Overview of directed energy deposition build and neutron diffraction measurements

Wang et al. [25] describe using DED to build four geometrically similar Inconel 625 thin-walled structures upon annealed substrates of the same material, as depicted in Fig. 1 (*Bottom Left*). Pre-alloyed gas atomized powder was delivered by a *Precitec YC-50* cladding head and melted by an *IPG Photonics YLR-12000* laser having a 4 mm spot diameter and a Gaussian beam profile [24]. A unidirectional laser path, as seen in Fig. 1 (*Right*), was used to deposit the even and odd layers of the build. Table 1 lists the DED parameters used. Given the thermomechanical nature of the DED process, with heat accumulation possibly affecting distortion, Wang et al. [25] assessed the influence of interlayer dwell time on the DED-induced distortion by imposing a 40 s dwell time after every layer in two of the four builds, while the remaining two builds were continuous, i.e., no interlayer dwell time.

Wang et al. subsequently used neutron diffraction (ND) measurements [26] to determine the lattice spacing and corresponding residual lattice strains along the {311} plane. Intergranular residual lattice strains along this plane have been found to be negligible for Inconel alloys [27], and hence any resulting stresses would reflect the macroscopic response.

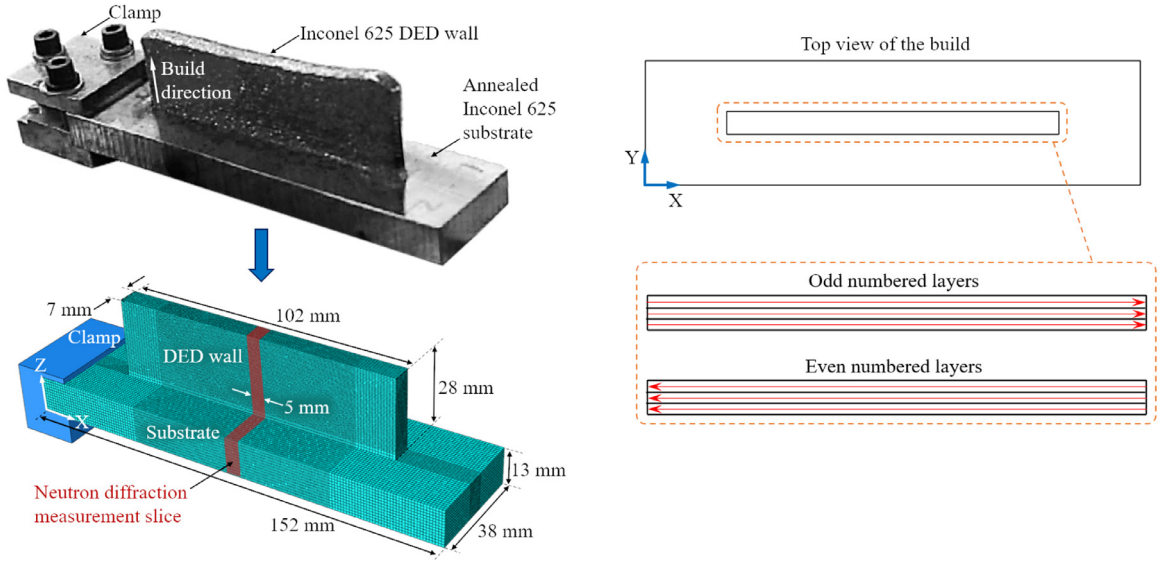

Fig. 1. (*Top Left*) Photograph of the Inconel 625 thin-walled structure built via directed energy deposition, adapted from [24] (*Bottom Left*) Finite element model depicting dimensions of the thin-walled Inconel 625 structure. The red colored slice represents the region used for neutron diffraction measurements by Wang et al. [25]. (*Right*) Laser scan path for even and odd layers. (For interpretation of the reference to color in this figure, the reader is referred to the online version of this article.)

Table 1
Directed energy deposition process parameters [24,25].

DED Parameters	Value
Laser power	2000 W
Laser speed	10.6 mm s^{-1}
Powder feed rate	16 g min^{-1}
Powder diameters	44 to 149 μm
Argon gas flow rate	9.4 L min^{-1}
Beads per layer	3
Deposition path	±X (ref. Fig. 1)
Bead width	2.29 mm
Bead thickness	0.89 mm

For details related to the ND facility/equipment, the reader is referred to [28,29]. Considering the symmetry and DED build parameters of the thin-walled structure, they assumed that the principal stress directions would align with the Cartesian coordinate system illustrated in Fig. 1. Based on this assumption the normal residual stress (RS) components were calculated. Shear stresses were not documented, and the normal stress in the Y direction (through thickness direction) was found to be on the order of the ND measurement uncertainty and was therefore not discussed. From Wang et al.'s work, only two components of the residual stress field, i.e., σ_X and σ_Z, were thus provided, while the others remain unknown. Furthermore, these two components were calculated within a 5 mm "slice", as indicated in Fig. 1 (*Bottom Left*). To predict the full continuum-level residual stress field in the entire wall, they executed a thermomechanical Lagrangian finite element (FE) model of the DED process. Comparison of their numerically predicted stress components with those obtained via ND measurements revealed that the numerical model could capture trends in the RS reasonably well, although significant differences were seen in the magnitudes of the predicted and measured RS components.

Thermomechanical FE models are widely used for simulating the full RS field in AM processes, as represented in published literature [30–37], although it should be noted that larger build volumes can prohibitively increase the computational expense. Mesh coarsening strategies have been documented to drastically improve computational efficiency with negligible loss in accuracy [38–42], however, as build volumes get larger, these simulations will inevitably become excessively time-consuming. An alternative approach to FE simulation for generating the full-geometry residual stress field is proposed and demonstrated in this work. The iterative stress reconstruction algorithm (ISRA) [43–46] is applied which, as discussed next, can be used to reconstruct a compatible stress field with either: (1) spatially limited experimental measurements, or (2) experimental measurements with incomplete stress field information, or (3) both, as is the case with Wang et al.'s work, wherein only σ_X and σ_Z are known at the centrally located slice. Used in the demonstrated work are RS components calculated from their ND measurements on continuous builds where reference samples were not heat treated.

2.2. Residual stress reconstruction

Some of the most promising approaches toward RS reconstruction include (1) the inverse eigenstrain method [47–49], (2) Eigenstrain-free methods using Airy stress functions [50–54], and (3) the iterative stress reconstruction algorithm (ISRA) [44–46]. The inverse eigenstrain method and Airy stress function approach are difficult to apply when the required number of basis functions significantly increases, as is the case with large three-dimensional stress distributions [55]. Moreover, implementing appropriate basis functions requires a priori knowledge of the eigenstrain distribution. Considering that metal AM components can vary in size and intricacy, complex RS distributions may exist, and thus a great number of experimental measurements is needed before the inverse eigenstrain method or Airy stress function approach can be appropriately used. In contrast, ISRA works well in this regard given its insensitivity to factors such as limited spatial resolution and coverage of experimental measurements, as well as incomplete stress tensors (incomplete fields) at measurement locations. This is important considering that RS in critical/specific regions of interest may be sought, rather than RS in the entire additive build. Considering the limited RS data available from Wang et al.'s ND measurements, ISRA is implemented to obtain a complete (and compatible) RS field for the entire DED build.

The flowchart presented in Fig. 2 illustrates how ISRA is applied in the demonstrated work. A Lagrangian, static, nonlinear-displacement based FE equilibration model, whose geometry is depicted in Fig. 1, is created to replicate the full RS field in the DED build. Initially, the RS field for the entire model is set to zero ($\boldsymbol{\sigma}_{ij}{}^{0} = \mathbf{0}$). Elements, $\mathbf{E}^{m}$, spa-

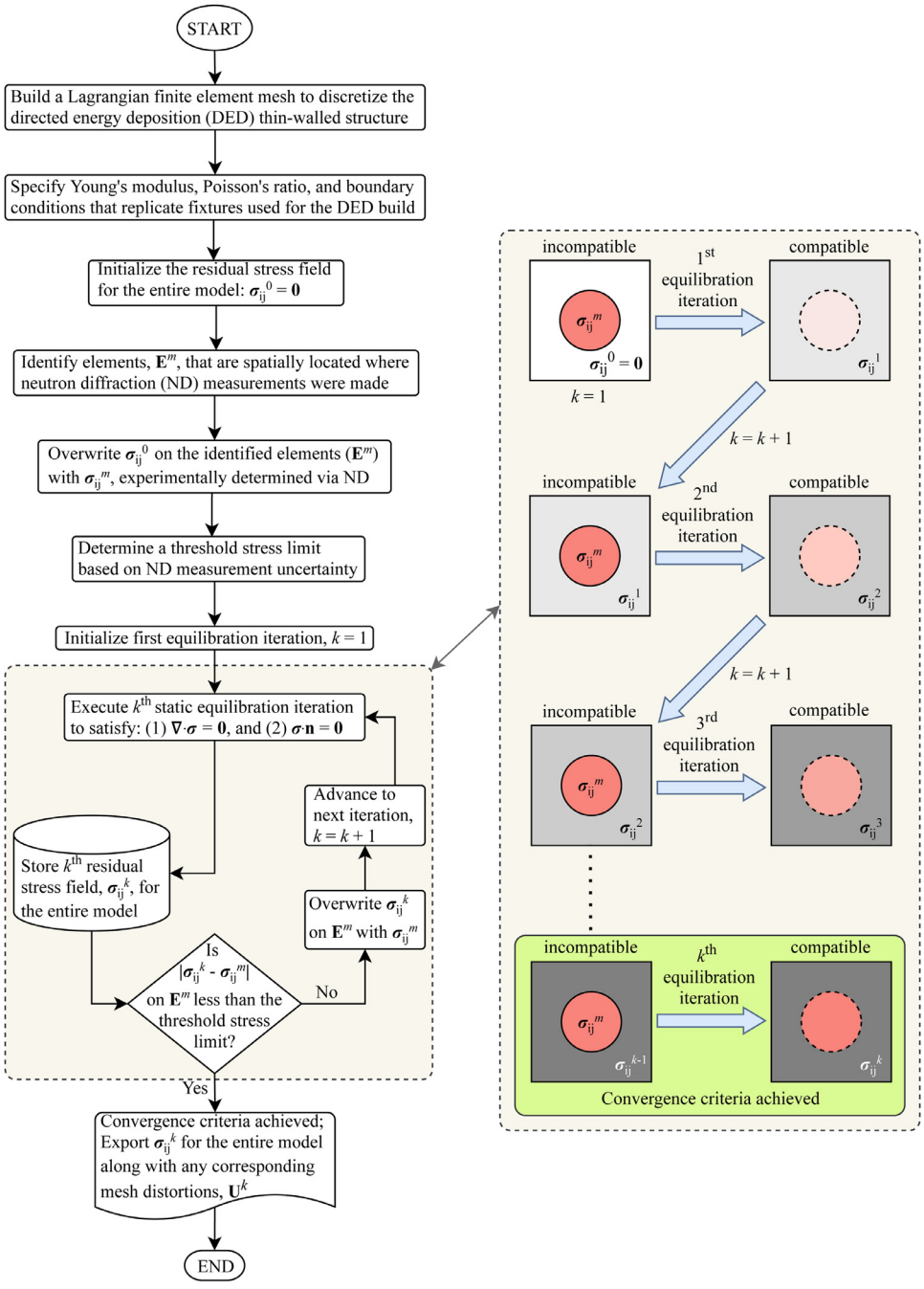

Fig. 2. Flowchart depicting the iterative stress reconstruction algorithm (ISRA).

tially located wherever ND measurements were made, are identified and overwritten with the measured RS field, σ_{ij}^m, determined via ND. This initially creates an incompatible state of stress for the entire model. The first static equilibration iteration ($k = 1$) is then executed such that stress equilibrium conditions are satisfied and a compatible stress distribution is obtained. Equilibration is based on the strain compatibility condition described by Eq. (1) [56,57].

$$\nabla \times (\nabla \times \boldsymbol{\varepsilon}_T)^{\intercal} = \mathbf{0} \tag{1}$$

Note that the linearized total strain in a solid body, $\boldsymbol{\varepsilon}_T$, can be decomposed into the elastic strain, $\boldsymbol{\varepsilon}$, and inelastic eigenstrain, $\boldsymbol{\varepsilon}^*$, as seen in Eq. (2).

$$\boldsymbol{\varepsilon}_T = \boldsymbol{\varepsilon} + \boldsymbol{\varepsilon}^* \tag{2}$$

Substituting Eq. (2) in Eq. (1), the strain compatibility equation can be expressed in terms of elastic strain and eigenstrain components, as given by Eq. (3). Neither the elastic nor inelastic strains needs to be compatible, however, the total strain does require compatibility.

$$\nabla \times (\nabla \times \boldsymbol{\varepsilon})^{\intercal} + \nabla \times (\nabla \times \boldsymbol{\varepsilon}^*)^{\intercal} = \mathbf{0} \tag{3}$$

From Eq. (3) it is inferred that any distribution of $\boldsymbol{\varepsilon}^*$ that introduces finite forcing terms will trigger a finite and incompatible distribution of $\boldsymbol{\varepsilon}$. For linear-elastic materials, the three-dimensional elastic stress tensor, $\boldsymbol{\sigma}$, can be expressed in terms of $\boldsymbol{\varepsilon}$ and the material stiffness tensor $\boldsymbol{C}$, as given by Eq. (4).

$$\boldsymbol{\sigma} = \boldsymbol{C} : \boldsymbol{\varepsilon} \tag{4}$$

Given Eqs. (3) and (4), knowledge of $\boldsymbol{\varepsilon}^*$ and $\boldsymbol{C}$ are sufficient to compute the RS distribution in the solid body. A compatible stress distribution can be calculated for the entire body by solving Eq. (3) and (4) whilst simultaneously satisfying Eq. (5) and (6). The latter provide conditions

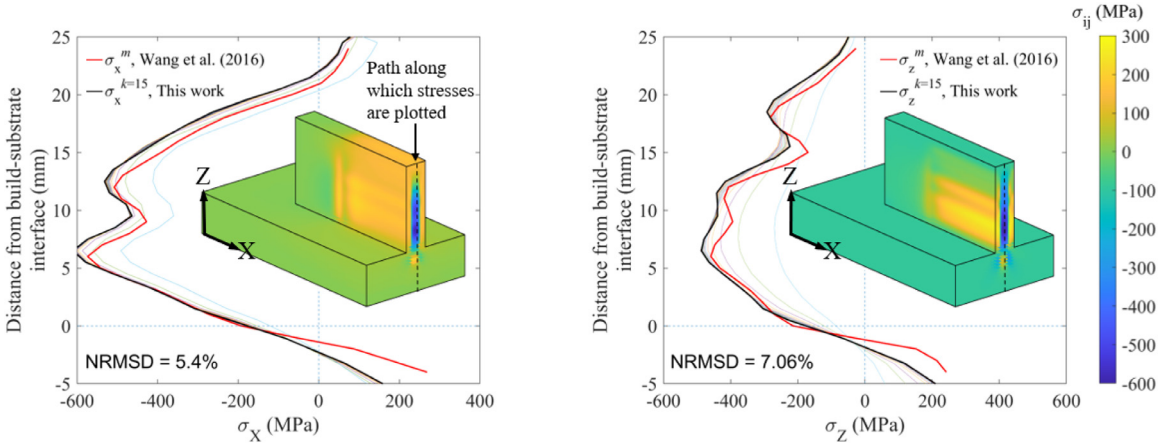

Fig. 3. Comparison of the reconstructed stress fields ${\sigma_X}^k$ and ${\sigma_Z}^k$ after 15 iterations (k = 15), with those determined by Wang et al. [25] via neutron diffraction measurements. This comparison is made along a path formed by the intersection of the central X and Y planes, as depicted in the inset images. The inset images present a three-dimensional perspective of the reconstructed σ_X and σ_Z distributions after 15 iterations. The faint lines plotted represent results of iterations prior to convergence. (For interpretation of the reference to color in this figure, the reader is referred to the online version of this article.)

for translational equilibrium and force equilibrium, respectively. The moment equilibrium is automatically satisfied by considering symmetry in the stress matrix (Eq. (7)), i.e., six independent components of stress.

$$\nabla \cdot \boldsymbol{\sigma} + \mathbf{f_B} = \mathbf{0} \tag{5}$$

$$\boldsymbol{\sigma} \cdot \mathbf{n} = \mathbf{0}, \quad \text{on surface } \boldsymbol{S} \tag{6}$$

$$\boldsymbol{\sigma} = \boldsymbol{\sigma}^{\mathsf{T}} \tag{7}$$

In Eqs. (5) and (6), $\mathbf{f_B}$ is the body force per unit volume (not considered herein), and $\mathbf{n}$ is the unit outward normal to the surface, $\boldsymbol{S}$, bounding the volume. By imposing the experimentally determined (incompatible) stress field, ${\sigma_{ij}}^m$, on $\mathbf{E}^m$, a compatible RS field, ${\sigma_{ij}}^k$, over the entire body can be computed via equilibrium iterations. Multiple iterations are required since the imposed stresses change during equilibration and hence need to be reimposed at the same spatial locations. The iterative process terminates once the absolute difference between ${\sigma_{ij}}^k$ and ${\sigma_{ij}}^m$ (on $\mathbf{E}^m$) is less than a predetermined threshold stress limit that accounts for the uncertainty in ND measurements. A Python script is used to implement the algorithm. Once convergence is achieved, the final ${\sigma_{ij}}^k$ is representative of the reconstructed stress field.

Considering the milling simulation that follows, a biased linear hexahedral mesh is incorporated, as seen in Fig. 1. Finer, cubic elements having an edge length, L_e, of 0.5 mm discretize the region of the wall to be machined, while coarser elements (L_e = 1 mm) discretize the remaining regions. For the iterative equilibration algorithm, only the Young's modulus, 156.3 GPa, and the Poisson's ratio, 0.36, at room temperature along the {311} plane are implemented in the material definition [25,58]. The stress reconstruction simulation only requires translational degrees of freedom, and solutions to the equilibrium equations, depicted in Fig. 3, are obtained using the implicit solver of Abaqus v6.14. With insufficient measurement data, the challenge of non-uniqueness arises in the reconstructed stress; given the absence of ND data elsewhere in the DED build, ISRA still converges to reveal a compatible RS distribution, however, this reconstructed distribution may not necessarily reflect the actual distribution for stress components at locations not represented by the ND measurement data. Therefore, in lieu of additional ND data, the overall spatially distributed RS contour patterns exhibited in a separate Inconel 625 DED simulation by Li et al. [40], but featuring similar geometry and deposition pattern, are also examined. The RS components from ND are subsequently imposed along the longitudinal (scan) and transverse directions of the thin-walled structure, within the finely meshed region (ref. Fig. 1), to replicate the trends predicted by [40]. While the accuracy of Li et al.'s predictions no doubt influences the reconstructed RS in the demonstrated FE model, their use is justified considering that the overarching goal of this work is to examine the effect of metal additive manufacturing RS on post-process machining-induced stress and distortion, rather than rigorous prediction and validation of the DED-induced RS.

Li et al.'s [40] decoupled thermal and mechanical analyses (using Netfabb) [59], with a mesh coarsening strategy set to 2 fine layers, when run on a 24 core Intel Xeon system equipped with 192 GB RAM, completed in 30 minutes (combined), with a reported prediction error of less than 5%. In comparison, the solution via ISRA presented in Fig. 3 converges in 15 iterations (k = 15) that are computed in 10 minutes using one Intel i7 4790 processor (3.6 GHz) with 32 GB RAM, revealing normalized root mean square difference (NRMSD) of 5.4% and 7.06%, respectively, for the σ_X and σ_Z distributions. Note that RMSDs have been normalized by dividing by the respective ND stress component's range, i.e., the normalizing denominator is $|\max(\sigma_i) - \min(\sigma_i)|$. While this demonstrates the efficiency of ISRA, a direct comparison can be misleading as ISRA requires some experimental measurements prior to execution that may necessitate time consuming data acquisition.

Given the limited ND data used from Wang et al. [25], the full converged RS field may differ somewhat to that numerically predicted by Li et al. [40], however, RS in the finely meshed region of the wall (ref. Fig. 1), where machining is to be simulated here, is reconstructed to closely resemble the two stress components determined by ND. This comparison is made considering the σ_X and σ_Z distributions along a path formed by the intersection of the central X and Y planes, as depicted in the inset images in Fig. 3. The intermediate stress profiles during iterations prior to convergence are also shown (as faint lines). Note that the DED RS distributions seen in the inset images are symmetric about the central X and Y planes. This reconstructed stress field is now implemented as an initial state in the high-speed end milling simulation, as described next.

3. High-speed end milling simulation

To simulate RS and distortion within the DED build during high-speed end milling, the Lagrangian FE mesh described in Section 2 (ref. Fig. 1) is discretized with elements featuring both temperature and displacement degrees of freedom. Material removal is implemented via element deletion based on a linear-deformation failure criterion. Temperature dependent material properties for Inconel 625 are applied together with a Johnson-Cook (J-C) plasticity definition [60], in conjunction with ductile and shear damage models, described next.

3.1. Material model and damage criteria

Temperature dependent thermal properties including thermal conductivity, density, Young's modulus, Poisson's ratio, thermal expansion coefficient, and specific heat have been referenced from [25,61,62]. The J-C plasticity model described by Eq. (8) and (9) has been widely used for orthogonal milling/turning simulations given its ability to capture the influence of temperature and strain rate on flow stress of the material [63–67].

$$\sigma_f = \left[A + B(\varepsilon^{pl})^n\right]\left[1 + C\ \ln\left(\frac{\dot{\varepsilon}^{pl}}{\dot{\varepsilon}_0}\right)\right]\left[1 - \left(T^*\right)^m\right] \tag{8}$$

$$T^* = \begin{cases} 0, & T < T_0 \\ \left(\dfrac{T - T_0}{T_m - T_0}\right) & T_0 \le T \le T_m \\ 1, & T > T_m \end{cases} \tag{9}$$

In Eqs. (8) and (9), σ_f is the flow stress, A is the quasi-static yield stress, B is the strain hardening coefficient, C is the strain-rate hardening coefficient, ε^{pl} is the plastic strain, $\dot{\varepsilon}^{pl}$ is the plastic strain rate, $\dot{\varepsilon}_0$ is the reference strain rate, n is the strain hardening exponent, m is the thermal softening exponent, and T^* is the homologous temperature term. Parameters for the J-C constitutive model, determined by Hokka et al. [63] via split Hopkinson pressure bar experiments, are provided in Table 2.

During the milling simulation, along the tool-workpiece interface, ductile and/or shear fracture may occur. Phenomenological observations made by Hooputra et al. [69] have revealed the importance of considering both failure mechanisms. Thus, the demonstrated milling simulation implements competing ductile and shear damage initiation criteria in conjunction with the J-C plasticity definition.

The ductile, Johnson-Cook, and shear damage initiation criteria are implemented simultaneously. At every time increment during the simulation, each criterion will independently compute a (normalized) state variable for every element. An initiation criterion is met once its state variable reaches a value of unity. At this point, the material stiffness for the affected element(s) is consequently degraded via a predetermined damage evolution law per the specific criterion.

The ductile damage criterion described by Eqs. (10), (11) and (12) phenomenologically predicts the onset of damage due to void nucleation, void growth and coalescence of porosities. It defines equivalent plastic strain at the onset of damage, γ_D, as a function of stress triaxiality, η, and plastic strain rate, $\dot{\varepsilon}^{pl}$. The ductile criterion state variable, ω_D, monotonically increases with the onset of plastic deformation until Eq. (10) is satisfied. Eq. (11) computes the increase in the ductile criterion state variable, $\Delta\omega_D$, with successive time increments during the simulation.

$$\omega_D = \int \frac{d\varepsilon^{pl}}{\gamma_D(\eta, \dot{\varepsilon}^{pl})} = 1 \tag{10}$$

Table 2
Johnson-Cook plasticity parameters for Inconel 625 implemented in the milling simulation [63,68].

J-C Parameters	Value (Inconel 625)
A	558.8 MPa
B	2201.3 MPa
n	0.8
C	0.000209
m	1.146
$\dot{\varepsilon}_0$	1670 s^{-1}
T_0	296 K
T_m	1623 K

$$\Delta\omega_D = \frac{\Delta\varepsilon^{pl}}{\gamma_D(\eta, \dot{\varepsilon}^{pl})} \ge 0 \tag{11}$$

$$\eta = \frac{-p}{q} \tag{12}$$

The stress triaxiality, η, is defined by Eq. (12), where p is the average stress and q is the equivalent von Mises stress. While dependence of γ_D on η has been well established [70–73], a relatively recent study from Bai and Wierzbicki [74] demonstrated that a three-dimensional asymmetric fracture locus may exist in the space of γ_D, η, and Lode angle, θ. Accordingly, the denominator term in Eqs. (10) and (11) would be rewritten as seen in Eq. (13), where ξ is the normalized third invariant of the deviatoric stress tensor, $\boldsymbol{\sigma}_s$, described by Eqs. (14) and (15), where r is the 3^{rd} invariant of deviatoric stress.

$$\gamma_D(\eta, \xi(\theta), \dot{\varepsilon}^{pl}), \quad -1 \le \xi(\theta) \le 1 \tag{13}$$

$$\xi = \left(\frac{r}{q}\right)^3 = \cos(3\theta) \tag{14}$$

$$r = \left(\frac{9}{2}\boldsymbol{\sigma}_s \cdot \boldsymbol{\sigma}_s : \boldsymbol{\sigma}_s\right)^{\frac{1}{3}} \tag{15}$$

The three-dimensional fracture locus (or fracture surface) has been found to improve prediction of ductile fracture in metals, however, this is not universally true for all metals. Bai and Wierzbicki validated their postulated asymmetric fracture locus with experiments performed on aluminum alloy 2024-T351 and A710 steel [75], however, they also reported that DH36 steel's fracture locus revealed no dependence on θ [74,76]. Algarni et al. [77] and Erice et al. [78] similarly reported a three-dimensional fracture locus for Inconel 718, wherein γ_D appeared far more sensitive to changes in η in comparison to changes in θ. For this reason, the influence of θ is not considered in the demonstrated work, albeit its importance in FE machining simulations, especially with regard to chip formation and geometry [66], should not be understated. A two-dimensional fracture locus relating η and γ_D is adopted herein based on tensile notch sensitivity experiments, performed with additively manufactured Inconel 625 cylindrical specimens, by Matache et al. [79].

While the ductile damage criterion described in Eq. (10) captures the influence of plastic strain rate, it does not capture the effect of temperature. Hence, the J-C damage criterion described by Eq. (16) is also applied [64,80,81].

$$\gamma_D = [D_1 + D_2 e^{D_3\eta}]\left[1 + D_4 \ln\left(\frac{\dot{\varepsilon}^{pl}}{\dot{\varepsilon}_0}\right)\right][1 + D_5 T^*] \tag{16}$$

In Eq. (16), D_1 is the initial fracture strain, $D_2 - D_5$ represent the exponential, triaxiality, strain-rate and temperature parameters, respectively [82]. The J-C damage parameters employed herein (ref. Table 3) were experimentally determined by Erice et al. [78].

The shear damage criterion described by Eqs. (17), (18) and (19) phenomenologically predicts the onset of damage via shear band localization, assuming equivalent plastic strain at the onset of damage, γ_s, to be function of shear stress ratio, τ_s (Eq. (19)), and plastic strain rate, $\dot{\varepsilon}^{pl}$. The shear criterion state variable, ω_s, monotonically increases with the onset of plastic deformation proportional to the incremental

Table 3
Johnson-Cook damage parameters implemented in the milling simulation [78,83].

D_1	D_2	D_3	D_4	D_5
0.04	0.75	-1.45	0.04	0.89

change in γ_s, until Eq. (17) is satisfied. Eq. (18) computes the increase in the shear criterion state variable, $\Delta\omega_s$, with successive time increments during the simulation. In Eq. (19), τ_{max} is the shear stress limit defined as $0.577A$ per distortion-energy theory, and material parameter k_s is assigned to be 1.57 [84].

$$\omega_s = \int \frac{d\varepsilon^{pl}}{\gamma_s(\tau_s, \dot{\varepsilon}^{pl})} = 1 \tag{17}$$

$$\Delta\omega_s = \frac{\Delta\varepsilon^{pl}}{\gamma_s(\tau_s, \dot{\varepsilon}^{pl})} \geq 0 \tag{18}$$

$$\tau_s = \frac{(q + k_s p)}{\tau_{max}} \tag{19}$$

The damage evolution expression given by Eq. (20) describes the rate of degradation of material stiffness, when any of the aforementioned damage initiation criteria are met. In Eq. (20), $\boldsymbol{\sigma}$ is the incrementally computed stress tensor, $\boldsymbol{\sigma}^*$ is the undamaged stress tensor and D is the overall damage variable such that the load-carrying capacity of a material is lost when D = 1. When D = 0.9 at the integration point of an element, the corresponding element is deleted from the mesh. Note, since reduced integration is employed in the demonstrated work, each element has only one integration point, located at its centroid.

$$\boldsymbol{\sigma} = (1 - D)\boldsymbol{\sigma}^* \tag{20}$$

To accommodate multiple damage criteria, the overall damage variable is determined by the greatest individual damage variable, d_j, corresponding to the j^{th} damage criteria, at a given increment of time, as described by Eq. (21).

$$D = \max(d_j) \tag{21}$$

Once damage initiates, the linear damage evolution law described by Eq. (22), defines the relationship between plastic distortion rate, $\dot{U}^{pl}$, characteristic element length, L_e, rate of change of the specific damage variable, $\dot{d}_j$, plastic strain rate, $\dot{\varepsilon}^{pl}$, and effective plastic distortion at the point of failure, U_f^{pl}. After damage initiation, if the material response is assumed perfectly plastic, i.e., constant yield strength, the predicted stress-strain softening response will be truly linear.

$$\dot{d}_j = \frac{L_e \dot{\varepsilon}^{pl}}{U_f^{pl}} = \frac{\dot{U}^{pl}}{U_f^{pl}} \tag{22}$$

3.2. Tool geometry, boundary conditions and tool paths

Since the goal of this work is to examine the effect of metal additive manufacturing RS from DED on the post-process machining-induced stress and distortion within the part, the milling tool is modeled as a discrete rigid shell. This avoids calculation of the stresses arising in the tool, thereby reducing computation time. The tool is meshed using rigid bilinear quadrilateral elements with an approximate length of 1 mm. Details regarding the tool geometry and high-speed machining parameters used in the simulation are listed in Table 4.

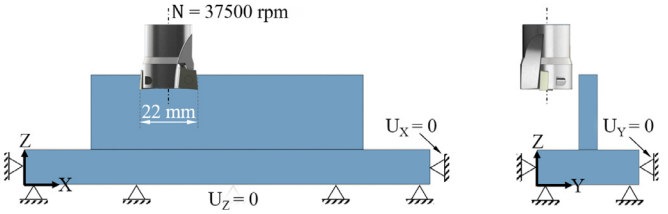

Fig. 4. Boundary conditions applied to the DED build during the milling simulation.

Table 4
Milling tool geometry and high-speed machining parameters [85,86].

Parameters	Value
Cutting diameter	22 mm
Number of inserts	2
Axial rake angle	0° (neutral)
Radial rake angle	0° (neutral)
Spindle speed, N	37500 rpm
Feed, f_N	0.16 mm rev^{-1}
Axial depth of cut	5 mm

The tool is assigned an angular velocity, ω_Z, about its vertical (Z) axis as well as a feed, V_f, as specified by Eqs. (23), (24).

$$\omega_Z = \frac{2\pi N}{60} \approx 3900 \text{ rad s}^{-1} \tag{23}$$

$$V_f = f_N N = 6 \text{ m min}^{-1} \tag{24}$$

The heat flux generated via Coulomb friction, Q_f, described in Eq. (25), is a function of the plastic heat dissipation fraction, Ψ, the coefficient of friction, μ, contact pressure at the tool-workpiece interface, p_c, and slip rate, $\dot{s}$ [87]. Ψ is assumed 90% herein, per [88].

$$Q_f = \Psi \mu p_c \dot{s} \tag{25}$$

Heat flux per unit volume Q_p, resulting from plastic strain heat dissipation in the DED build during the milling operation, is defined by Eq. (26).

$$Q_p = \Psi \boldsymbol{\sigma} : \dot{\varepsilon}^{pl} \tag{26}$$

Boundary conditions are imposed on five orthogonal faces of the substrate, constraining translational motion, as seen in Fig. 4.

To study the effects of the DED RS on the milling-induced stress and distortion, the converged (and compatible) residual stress, $\boldsymbol{\sigma}_{ij}{}^k$, and any corresponding mesh distortions, $\mathbf{U}^k$, obtained from ISRA are implemented as initial conditions for the milling simulation, described by

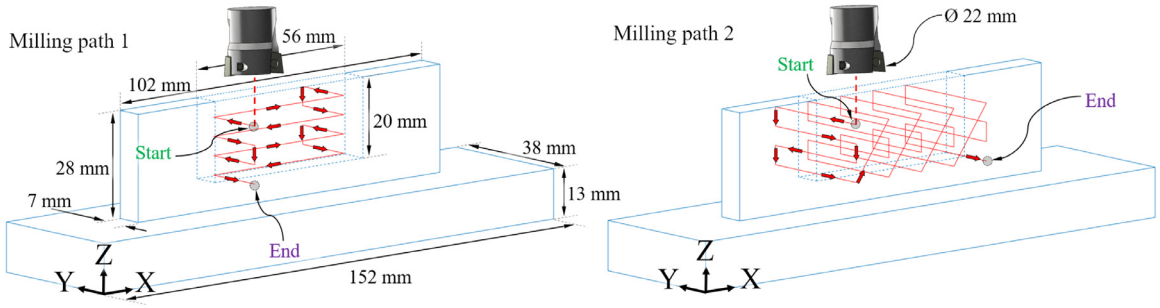

Fig. 5. Tool paths considered in the milling simulations. Net volume of material to be removed (dotted line) is the same in both cases.

Eqs. (27) and (28).

$$\boldsymbol{\sigma}(\mathbf{X}, 0) = \boldsymbol{\sigma}_{\mathrm{ij}}^{k}(\mathbf{X}) \tag{27}$$

$$\mathbf{U}(\mathbf{X}, 0) = \mathbf{U}^{k}(\mathbf{X}) \tag{28}$$

To elucidate how much of a difference consideration of the DED RS makes, an identical case is executed wherein the DED RS is not considered, i.e., no initial conditions are applied, resulting in zero RS within the part prior to machining. In addition, two different tool path strategies, both of which generate the same cut in the thin-walled region, are examined as seen in Fig. 5. The aim of this, as stated earlier, is to observe how much of a difference (if any) arises in the respective machining-induced stress and distortion, and the extent to which the DED RS consideration affects this observation, given the general magnitude of the DED-induced RS.

Solutions for the described milling simulations are computed using the explicit solver of Abaqus v6.14. Results for both milling patterns, with and without considering the DED-induced RS in the workpiece, are presented and discussed next.

4. Results and discussion on the effect of DED residual stress on post-process machining-induced stress and distortion

A comparison of trends in the milling-induced RS, for both milling paths 1 (M1) and 2 (M2), considering the presence or absence of DED RS, can now be made. Residual stress comparisons are quantitatively made along both the vertical and horizontal paths as seen in Fig. 6, and are presented via the plots in Figs. 7 and 8. In both Figs. 7 and 8, a qualitative comparison of the overall distributions of the normal stress within the structure is also provided when considering DED RS (3D contours).

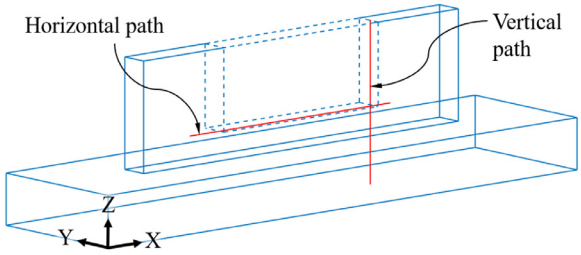

Fig. 6. Vertical path connecting points (104.5, 19, 0) mm and (104.5, 19, 41) mm and horizontal path connecting points (43, 19, 20.5) mm and (108, 19, 20.5) mm along which the predicted normal stress components are probed.

Trends observed are summarized as follows:

1. Despite the symmetric DED RS field imposed as an initial condition (ref. Fig. 3) the milling-induced RS reveals an asymmetric distribution. Furthermore, differences in the distribution of compressive and

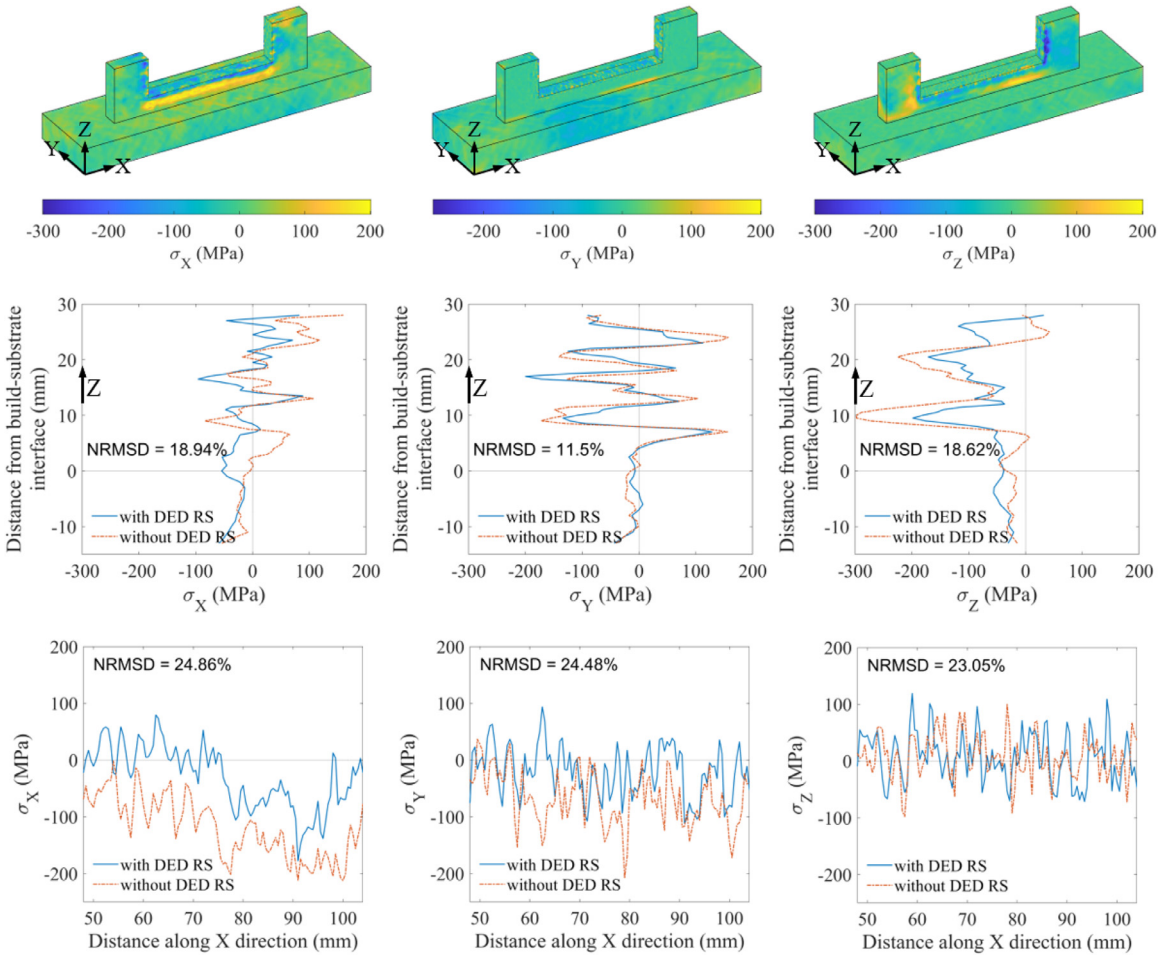

Fig. 7. Residual stress predicted from milling path 1 (M1). (*Above*) A 3D view illustrating the distributions of normal stress components, considering DED RS. (*Center*) Distribution of normal stress components along a vertical path with and without considering DED RS. (*Below*) Distribution of normal stress components along a horizontal path with and without considering DED RS. (For interpretation of the reference to color in this figure, the reader is referred to the online version of this article.)

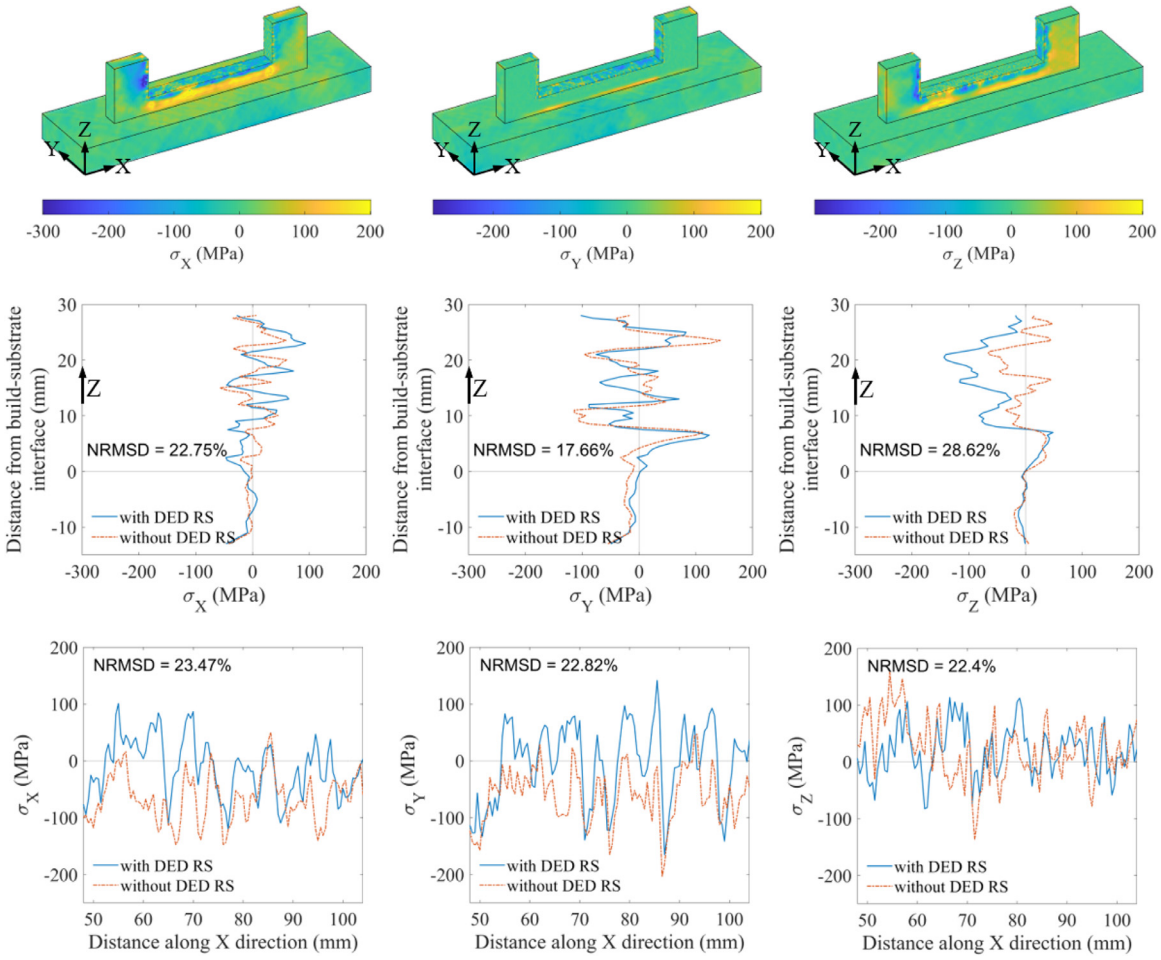

Fig. 8. Residual stress predicted from milling path 2 (M2). (*Above*) A 3D view illustrating the distributions of normal stress components, considering DED RS. (*Center*) Distribution of normal stress components along a vertical path with and without considering DED RS. (*Below*) Distribution of normal stress components along a horizontal path with and without considering DED RS. (For interpretation of the reference to color in this figure, the reader is referred to the online version of this article.)

tensile milling-induced RS along the surface of the cut are evident when comparing M1 and M2.

2. The peak compressive residual stress measured via neutron diffraction was approximately -600 MPa and -400 MPa for σ_X and σ_Z, respectively (ref. Fig. 3), however following the milling operation, the state of compressive residual stress is significantly reduced for the same components, with peaks approaching -300 MPa near the edges of the cut.
3. For both M1 and M2, similar trends are predicted with and without considering DED RS along the vertical path, with aperiodic patterns of alternating tensile and compressive stress. Subtle differences are noticed when comparing the ranges of these aperiodic patterns in the milling-induced σ_X and σ_Y; in both cases M1 and M2, an approximate range of -100 to 100 MPa is predicted for σ_X, while an approximate range of -200 to 150 MPa is predicted for σ_Y. There is, however, a significant difference when comparing the range in σ_Z predicted for M1 and M2; in the case of M1, σ_Z varies from about -300 MPa to 40 MPa when DED RS is neglected, whereas the corresponding range reduces to approximately -50 MPa to 50 MPa in the case of M2. When DED RS is considered, however, σ_Z varies from about -200 MPa to 40 MPa in the case of M1, whereas the range is reduced to approximately -150 MPa to 50 MPa for M2.
4. Comparing the normalized root mean square difference (NRMSD) between the milling-induced RS, with and without DED RS, along the vertical path for M1 and M2, significant differences are observed. The NRMSD is 18.94%, 11.5%, and 18.62% for σ_X, σ_Y, and σ_Z respectively, in the case of M1, whereas, for M2, the respective differences increase significantly to 22.75%, 17.66%, and 28.62%.
5. Interestingly, the observations made along the vertical path are slightly reversed along the horizontal path; considerable differences are noticed when comparing the range of the aperiodic patterns in milling-induced σ_X and σ_Y; In the case of M1, σ_X varies from about -200 MPa to 0 MPa without considering DED RS, whereas the range shifts to approximately -150 MPa to 50 MPa in the case of M2. When DED RS is considered, σ_X varies from about -170 MPa to 80 MPa for M1, whereas the range reduces to about -120 MPa to 100 MPa for M2. For both M1 and M2, σ_Y varies from around -200 MPa to 40 MPa without considering DED RS, whereas when DED RS is considered, σ_Y varies from approximately -100 MPa to 100 MPa in the case of M1, while the range increases to -160 MPa to 130 MPa for M2. The range of the aperiodic patterns in milling-induced σ_Z, in the case of M1, is between approximately -100 MPa to 100 MPa, with and without consideration of DED RS. In the case of M2, this range increases noticeably to -140 MPa to 155 MPa when DED RS is not considered.
6. Along the horizontal path, NRMSD for the normal stress components does not vary significantly between M1 and M2, although the magnitude of NRMSD is in the range of 22 to 25%, underscoring the difference in the predictions due to inclusion of the DED RS.

From magnitudes of NRMSD in milling-induced RS, along both the vertical and horizontal paths, it is evident that consideration of DED RS

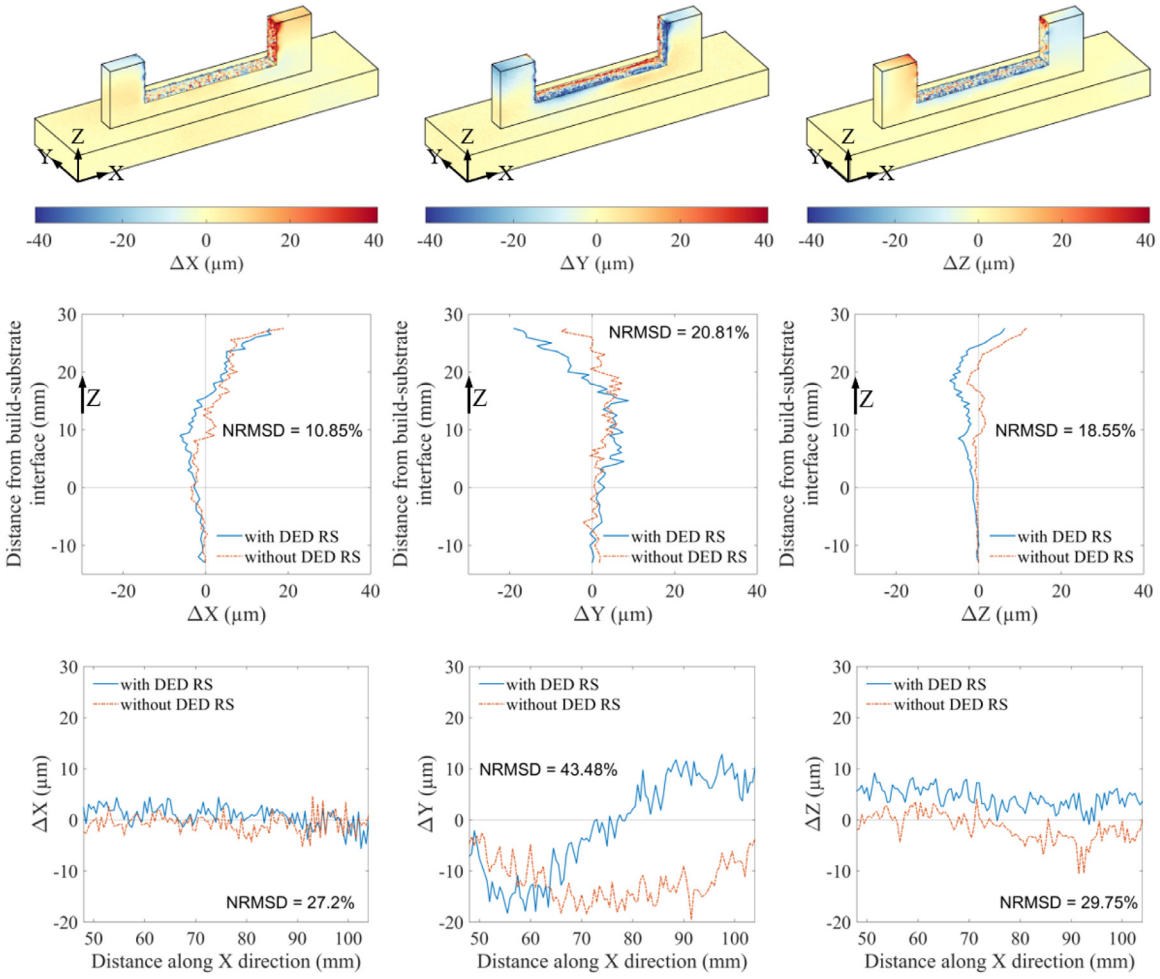

Fig. 9. Distortion generated via milling path 1 (M1). (*Above*) A 3D view illustrating the distributions of orthogonal distortion components, considering DED RS. (*Center*) Distribution of orthogonal distortion components along a vertical path with and without considering DED RS. (*Below*) Distribution of orthogonal distortion components along a horizontal path with and without considering DED RS. (For interpretation of the reference to color in this figure, the reader is referred to the online version of this article.)

makes a significant difference in the model's prediction, thus providing supporting evidence toward the first hypothesis. Variations are noticed in the aperiodic trends in RS, which alternate between compressive and tensile states, as well as in their overall range of RS. While an increase in peak compressive RS may improve the fatigue life of the part, an increase in the tensile RS undesirably achieves the opposite. The differences in NRMSD observed when comparing the RS distributions from M1 and M2, provides evidence in support of the second hypothesis, that the degree of influence of initial RS on machining-induce RS may vary with differences in tool path for the same net material removal. This helps illuminate the importance of appropriate tool path planning, to "engineer" a more desirable distribution of RS in the machined component, while simultaneously considering other factors such as machining cost.

Note that the RS information can also be obtained via experimental techniques, wherein one sample can be machined directly after printing while another can be heat-treated to relieve the DED-induced RS prior to machining. Neutron diffraction (ND) measurement might be of value considering its penetration depth and high resolution [26], however, uncertainty in the measurement needs be considered. The path lengths of individual neutrons passing through the specimen being examined vary throughout the gauge volume during ND measurement, and, given that absorption depends on distance traveled, detection can be biased toward the part of the gauge volume closest to the beam source [89], introducing uncertainty in the measurements of RS components. Goudar et al. [90] reported ND uncertainties ranging from ±15 MPa, near the surface of their 316 L cylindrical specimen, to as high as ±109 MPa for the axial stress component near the center of the cylinder. Given the differences in magnitudes of predicted machining-induced RS, with and without DED-induced RS consideration, as seen in Figs. 7 and 8, use of ND measurements with such high uncertainties may prove to be rather inconclusive in distinguishing any aperiodic trends in the RS distribution. Hence, considering the goals of the work, experimental measurement as such is not presented.

A comparison of trends in the milling-induced distortion, resulting from M1 and M2 considering the effect of DED RS, can be made from Figs. 9 and 10, respectively. In both figures, a comparison of the orthogonal distortion components within the 3D structure, when considering DED RS, is provided (*Above*), followed by the distributions of orthogonal distortion along a vertical path (*Center*) as well as along a horizontal path (*Below*). Trends observed are summarized as follows:

1. As expected, the free end of the wall has the most deflection (or distortion), however when comparing M1 with M2, significant differences in the distortion trends are observed regardless of influence of DED RS. This is especially evident with the distortion in the X direction (ΔX) and Y direction (ΔY), along the vertical and horizontal paths. Apart from differences in the overall distortion trends along these directions, the magnitudes of the peaks also differ, as is seen by comparison of Figs. 9 and 10.

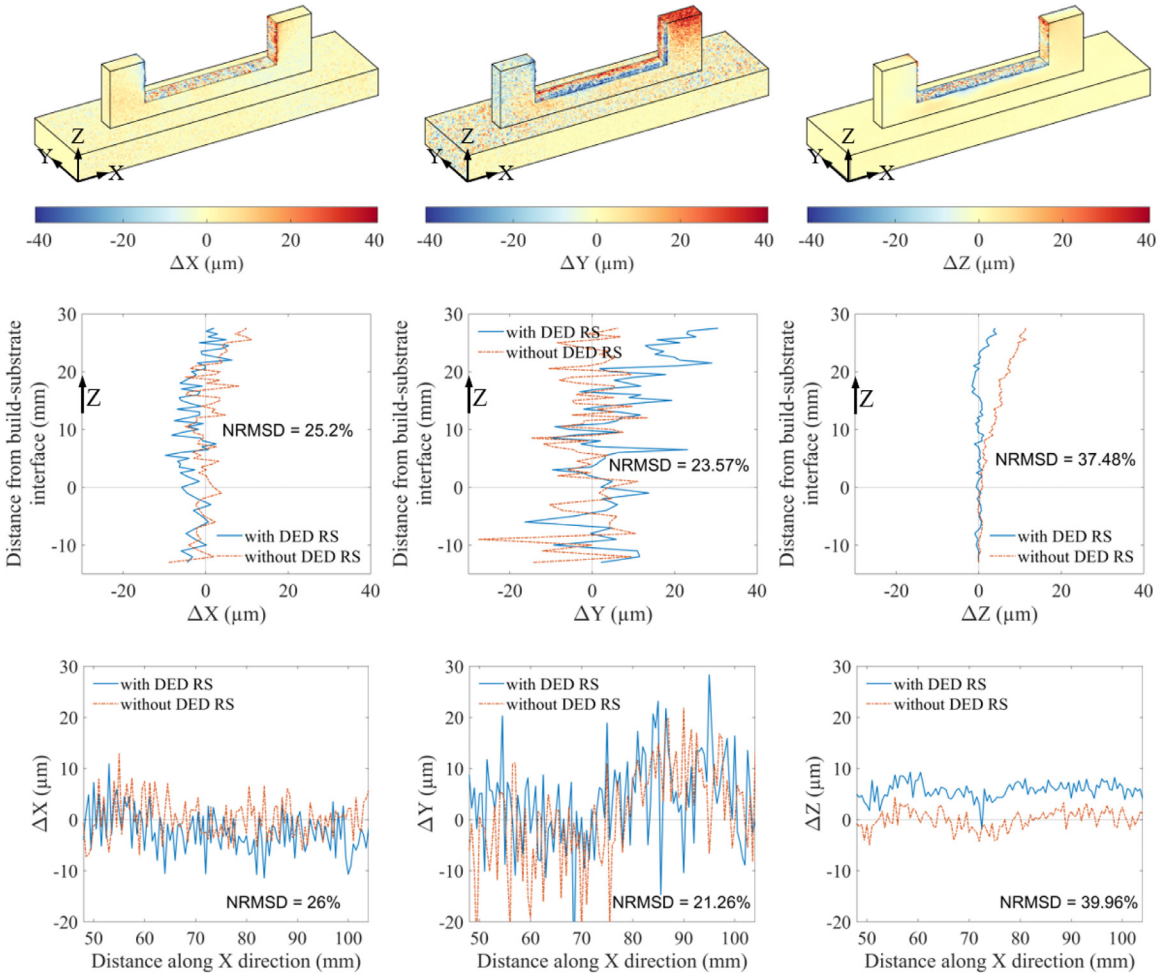

Fig. 10. Distortion generated via milling path 2 (M2). (*Above*) A 3D view illustrating the distributions of orthogonal distortion components, considering DED RS. (*Center*) Distribution of orthogonal distortion components along a vertical path with and without considering DED RS. (*Below*) Distribution of orthogonal distortion components along a horizontal path with and without considering DED RS. (For interpretation of the reference to color in this figure, the reader is referred to the online version of this article.)

2. The effect of considering DED RS is quantified from the distortion NRMSD observed along both the vertical and horizontal paths in case of M1 and M2; the NRMSD ranges from as little as 10% to almost 44% illuminating the significant influence that the DED RS has on the predicted milling-induced distortion. Comparing the NRMSD along the vertical paths of M1 and M2, the NRMSD is between 10 to 21% in the case of M1, and between 23 to 38% in the case of M2.
3. The distortion NRMSD for each orthogonal direction in M1 varies considerably from that of M2 indicating that the choice of tool path also has some influence on the differences in distortion observed when DED RS is considered.
4. With the introduction of DED RS, for both M1 and M2, a difference in trends between distortion parallel to build layers (ΔX and ΔY) and the distortion in the build direction (ΔZ) is predicted; While trends in ΔX and ΔY reveal significant overlap with and without DED RS, there is no overlap predicted for ΔZ along the vertical path in the thin wall, as well as along the horizontal path. along the horizontal path when considering the DED RS., is predicted to be 5 μm to 10 μm greater than that without considering the DED RS. It is plausible that this can be attributed to stress relief that occurs during the milling operation; referring to Fig. 3, the compressive RS is at its peak approximately 0.5 mm beneath the horizontal path (in the Z direction), and the state of compressive RS extends well above the horizontal path to regions from where the material is removed.

By comparing the differences in trends observed for M1 and M2, it is evident that the machining tool path has a significant effect on the net distortion of thin-walled components. Introducing RS from the additive manufacturing process can influence the distortion prediction to a certain degree, thus providing supporting evidence toward the first hypothesis. The amount of influence, however, appears to vary based on the choice of milling tool path, providing evidence in support of the second hypothesis, i.e., the degree of influence of initial RS on machining-induced part distortion varies with differences in tool path, for the same net material removal. In addition, the influence of stress relief is captured during the milling simulation by introducing the initial state of RS in the thin-walled structure that arises due to the rapid thermal cycles of the AM process.

From the aforementioned discussion it is evident that inclusion of the additive manufacturing-induced RS in the milling simulation has some degree of influence on the resulting stress and distortion. To help visualize the influence, an in-situ state of stress triaxiality, η, is presented for both M1 and M2 in Fig. 11. For both tool paths, there is a more uniform distribution of η in the thin-walled region of the build with the inclusion of DED RS. This difference in η, calculated during the milling simulation, can be expected considering the magnitude of DED-induced RS that is imposed as an initial condition, as presented earlier in Fig. 3, relative to the zero state of stress in the absence of DED-induced RS. For Inconel 625, the equivalent plastic strain resulting in ductile fracture increases with lower values of triaxiality [77]. In the presented milling

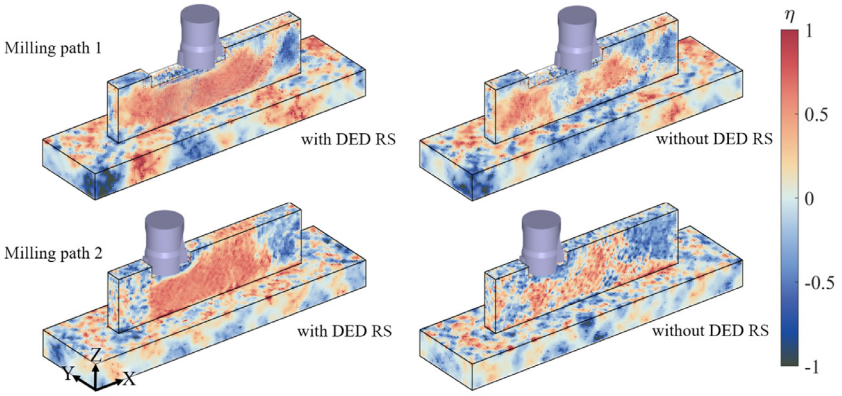

Fig. 11. Distribution of stress triaxiality during the milling simulation with and without considering DED RS. (*Above*) Stress triaxiality for milling path 1. (*Below*) Stress triaxiality for milling path 2. (For interpretation of the reference to color in this figure, the reader is referred to the online version of this article.)

simulations, the equivalent plastic strain in the workpiece is isolated to regions near the tool-workpiece interface where a dark blue region, indicative of low stress triaxiality, is predicted as seen in Fig. 11. Accordingly, the equivalent plastic strain along with the extent of damage computed influences the volume of material removal at the interface. For both M1 and M2, a region of low η appears to be localized near the tool-workpiece interface, when DED-induced RS is considered, whereas, a more spatially distributed region with relatively higher magnitudes is noticed when the DED-induced RS is not considered. The lower η predicted with the inclusion of DED RS, suggests an increased ductility and greater toughness in the material response. Thus, in addition to the differences observed for machining-induced RS and distortion, it is revealed that the inclusion of the AM-induced RS can also influence the material response, and therefore affect the volume of material being removed, during high-speed machining operations.

5. Conclusion

This work reveals the influence of metal additive manufacturing (AM) residual stress (RS) on post-process machining-induced stress and distortion. Limited RS field data obtained via neutron diffraction measurements for a directed energy deposition (DED) thin-walled structure are iteratively reconstructed and subsequently imposed as a compatible initial state for post-process high-speed milling simulations. Two different tool paths are simulated, both with and without inclusion of the RS field inherited from the DED process. The study reveals differences that arise in the machining-induced stress and part distortion according to the tool path variations, as well as the significant extent to which DED RS consideration affects this observation. Key findings from the study are summarized as follows:

- Normalized root-mean-square differences (NRMSD) of up to 25% and 29%, respectively, are observed in the high-speed machining-induced RS for two different tool paths when the DED inherent RS is considered. Likewise, maximum NRMSD of up to 44% and 40% are revealed in the post-machining distortion for the two respective machining strategies when DED RS is included. These results highlight the significance that RS generated during the DED build has on subsequent machining-induced RS and distortion.
- Differences observed when comparing the machining-induced RS distributions for the two tool paths examined underscores the importance of appropriate tool path planning to obtain more desirable distributions of RS in the machined component. Tool path design is also revealed to have a major effect on net distortion of the high-speed-machined DED build. Thus, introducing RS from the DED process is found to affect both distortion and induced residual stress during high-speed machining, however, the actual influence varies with the particular tool path strategy.
- Variations observed in the stress triaxiality computed during high-speed machining suggests that inclusion of RS from the DED process influences the localized response in the material near the tool-workpiece interface. Accordingly, the stress triaxiality variations can affect the volume of material removed during machining due to corresponding differences in the damage evolution.

The technical approach demonstrated in this work can be implemented for other AM and machining techniques, and can be extended to model fully-coupled, hybrid additive-subtractive manufacturing operations. With the capability to predict machining-induced RS and part distortion while accounting for RS in the bulk material (AM or otherwise), manufacturing cells can improve tool path planning and help deliver monolithic components that can be assembled with minimal correction.

Declaration of Competing Interest

The authors declare that they have no known competing financial interests or personal relationships that could have appeared to influence the work reported in this paper.

Acknowledgment

The authors acknowledge support in part from the U.S. National Science Foundation, grant no. CMMI-1762722. Any opinions, findings, or conclusions expressed in this paper are those of the authors and do not necessarily reflect the views of the U.S. National Science Foundation.

References

[1] Izamshah R, Mo J, Ding S. Hybrid deflection prediction on machining thin-wall monolithic aerospace components. Proceedings of the Institution of Mechanical Engineers, Part B: Journal of Engineering Manufacture 2012;226(4):592–605.
[2] Yang Y, Li M, Li K. Comparison and analysis of main effect elements of machining distortion for aluminum alloy and titanium alloy aircraft monolithic component. The International Journal of Advanced Manufacturing Technology 2014;70(9–12):1803–11.
[3] Chatelain J-F, Lalonde J, Tahan A. A comparison of the distortion of machined parts resulting from residual stresses within workpieces. In: Proceedings of the 4th International Conference on Manufacturing Engineering, Quality and Production Systems (MEQAPS11); 2011. p. 79–84.
[4] Chantzis D, Van-der Veen S, Zettler J, Sim W. An industrial workflow to minimise part distortion for machining of large monolithic components in aerospace industry. Procedia CIRP 2013;8:281–6.
[5] Li J-g, Wang S-q. Distortion caused by residual stresses in machining aeronautical aluminum alloy parts: recent advances. The International Journal of Advanced Manufacturing Technology 2017;89(1–4):997–1012.
[6] Mayr J, Jedrzejewski J, Uhlmann E, Donmez MA, Knapp W, Härtig F, et al. Thermal issues in machine tools. CIRP Ann 2012;61(2):771–91.
[7] Hussain A, Lazoglu I. Distortion in milling of structural parts. CIRP Ann 2019;68(1):105–8.
[8] Sridhar G, Babu PR. Effect of cutting parameters on machining induced distortion in thin wall thin floor parts. Journal of Mechanical Engineering (JMechE) 2019;16(1):59–78.
[9] Astakhov VP. The assessment of cutting tool wear. Int J Mach Tools Manuf 2004;44(6):637–47.
[10] Akhtar W, Sun J, Sun P, Chen W, Saleem Z. Tool wear mechanisms in the machining of nickel based super-alloys: a review. Frontiers of Mechanical Engineering 2014;9(2):106–19.

[11] Nowag L, Sölter J, Walter A, Brinksmeier E. Effect of machining parameters and clamping technique on residual stresses and distortion of bearing rings. Materialwissenschaft und Werkstofftechnik: Entwicklung, Fertigung, Prüfung, Eigenschaften und Anwendungen technischer Werkstoffe 2006;37(1):45–51.
[12] Richter-Trummer V, Suzano E, Beltrão M, Roos A, Dos Santos J, De Castro P. Influence of the FSW clamping force on the final distortion and residual stress field. Materials Science and Engineering: A 2012;538:81–8.
[13] Quintana G, Ciurana J. Chatter in machining processes: a review. Int J Mach Tools Manuf 2011;51(5):363–76.
[14] Advancing Aerospace Development with Metal 3D Printing Technology and Post-Processing. https://event.on24.com/wcc/r/2995356/247492E763F0BC54481579821E5E7E7D?; n.d., Accessed: 2021-03-16.
[15] Ma Y, Zhang J, Yu D, Feng P, Xu C. Modeling of machining distortion for thin-walled components based on the internal stress field evolution. The International Journal of Advanced Manufacturing Technology 2019;103(9):3597–612.
[16] Schajer GS. Practical residual stress measurement methods. John Wiley & Sons; 2013.
[17] Wang J, Zhang D, Wu B, Luo M. Prediction of distortion induced by machining residual stresses in thin-walled components. The International Journal of Advanced Manufacturing Technology 2018;95(9):4153–62.
[18] Schulze V, Arrazola P, Zanger F, Osterried J. Simulation of distortion due to machining of thin-walled components. Procedia Cirp 2013;8:45–50.
[19] Zhang Z, Zhang Z, Zhang D, Luo M. Milling distortion prediction for thin-walled component based on the average MIRS in specimen machining. The International Journal of Advanced Manufacturing Technology 2020;111(11):3379–3392.
[20] Becker B. Advanced machining toolpath for low distortion. Tech. Rep.. Third Wave Systems, Inc Eden Prairie United States; 2017.
[21] Sealy MP, Madireddy G, Williams RE, Rao P, Toursangsaraki M. Hybrid processes in additive manufacturing. J Manuf Sci Eng 2018;140(6).
[22] Beese AM, Carroll BE. Review of mechanical properties of ti-6Al-4V made by laser-based additive manufacturing using powder feedstock. Jom 2016;68(3):724–34.
[23] Chen Q, Liang X, Hayduke D, Liu J, Cheng L, Oskin J, et al. An inherent strain based multiscale modeling framework for simulating part-scale residual deformation for direct metal laser sintering. Addit Manuf 2019;28:406–18.
[24] Denlinger ER, Heigel JC, Michaleris P, Palmer T. Effect of inter-layer dwell time on distortion and residual stress in additive manufacturing of titanium and nickel alloys. J Mater Process Technol 2015;215:123–31.
[25] Wang Z, Denlinger E, Michaleris P, Stoica AD, Ma D, Beese AM. Residual stress mapping in inconel 625 fabricated through additive manufacturing: method for neutron diffraction measurements to validate thermomechanical model predictions. Materials & Design 2017;113:169–77.
[26] Kandil F, Lord J, Fry A, Grant P. A review of residual stress measurement methods. A Guide to Technique Selection, NPL, Report MATC (A) 2001;4.
[27] Holden T, Holt R, Clarke A. Intergranular strains in inconel-600 and the impact on interpreting stress fields in bent steam-generator tubing. Materials Science and Engineering: A 1998;246(1–2):180–98.
[28] Wang X-L, Holden T, Rennich GQ, Stoica A, Liaw PK, Choo H, et al. VULCANThe engineering diffractometer at the SNS. Physica B 2006;385:673–5.
[29] Ungár T, Stoica AD, Tichy G, Wang X-L. Orientation-dependent evolution of the dislocation density in grain populations with different crystallographic orientations relative to the tensile axis in a polycrystalline aggregate of stainless steel. Acta Mater 2014;66:251–61.
[30] Peyre P, Aubry P, Fabbro R, Neveu R, Longuet A. Analytical and numerical modelling of the direct metal deposition laser process. J Phys D Appl Phys 2008;41(2):025403.
[31] Neela V, De A. Three-dimensional heat transfer analysis of LENS TM process using finite element method. The International Journal of Advanced Manufacturing Technology 2009;45(9–10):935.
[32] Chiumenti M, Cervera M, Salmi A, De Saracibar CA, Dialami N, Matsui K. Finite element modeling of multi-pass welding and shaped metal deposition processes. Comput Methods Appl Mech Eng 2010;199(37–40):2343–59.
[33] Manvatkar V, De A, DebRoy T. Heat transfer and material flow during laser assisted multi-layer additive manufacturing. J Appl Phys 2014;116(12):124905.
[34] Michaleris P. Modeling metal deposition in heat transfer analyses of additive manufacturing processes. Finite Elem Anal Des 2014;86:51–60.
[35] Heigel J, Michaleris P, Reutzel EW. Thermo-mechanical model development and validation of directed energy deposition additive manufacturing of ti-6Al-4V. Addit Manuf 2015;5:9–19.
[36] Denlinger ER, Heigel JC, Michaleris P. Residual stress and distortion modeling of electron beam direct manufacturing ti-6Al-4V. Proceedings of the Institution of Mechanical Engineers, Part B: Journal of Engineering Manufacture 2015;229(10):1803–13.
[37] Liang X, Cheng L, Chen Q, Yang Q, To AC. A modified method for estimating inherent strains from detailed process simulation for fast residual distortion prediction of single-walled structures fabricated by directed energy deposition. Addit Manuf 2018;23:471–86.
[38] Denlinger ER, Gouge M, Irwin J, Michaleris P. Thermomechanical model development and in situ experimental validation of the laser powder-bed fusion process. Addit Manuf 2017;16:73–80.
[39] Gouge M, Denlinger E, Irwin J, Li C, Michaleris P. Experimental validation of thermo-mechanical part-scale modeling for laser powder bed fusion processes. Addit Manuf 2019;29:100771.
[40] Li C, Denlinger ER, Gouge MF, Irwin JE, Michaleris P. Numerical verification of an octree mesh coarsening strategy for simulating additive manufacturing processes. Addit Manuf 2019;30:100903.
[41] Jayanath S, Achuthan A. A computationally efficient finite element framework to simulate additive manufacturing processes. J Manuf Sci Eng 2018;140(4).
[42] Jayanath S, Achuthan A. A computationally efficient hybrid model for simulating the additive manufacturing process of metals. Int J Mech Sci 2019;160:255–69.
[43] Ficquet X. Development and application of the deep hole drilling method. University of Bristol; 2007.
[44] Do S, Serasli K, Smith D. Combined measurement and finite element analysis to map residual stresses in welded components. In: Pressure Vessels and Piping Conference, vol. 55713. American Society of Mechanical Engineers; 2013. V06BT06A065
[45] Coules H, Smith D, Venkata KA, Truman C. A method for reconstruction of residual stress fields from measurements made in an incompatible region. Int J Solids Struct 2014;51(10):1980–90.
[46] Chukkan JR, Wu G, Fitzpatrick ME, Jones S, Kelleher J. An iterative technique for the reconstruction of residual stress fields in a butt-welded plate from experimental measurement, and comparison with welding process simulation. Int J Mech Sci 2019;160:421–8.
[47] Qian X, Yao Z, Cao Y, Lu J. An inverse approach for constructing residual stress using BEM. Eng Anal Bound Elem 2004;28(3):205–11.
[48] Korsunsky A. Eigenstrain analysis of residual strains and stresses. The Journal of Strain Analysis for Engineering Design 2009;44(1):29–43.
[49] Song X, Korsunsky AM. Fully two-dimensional discrete inverse eigenstrain analysis of residual stresses in a railway rail head. J Appl Mech 2011;78(3).
[50] Farrahi G, Faghidian S, Smith D. An inverse approach to determination of residual stresses induced by shot peening in round bars. Int J Mech Sci 2009;51(9–10):726–31.
[51] Farrahi G, Faghidian S, Smith D. Reconstruction of residual stresses in autofrettaged thick-walled tubes from limited measurements. Int J Press Vessels Pip 2009;86(11):777–84.
[52] Farrahi G, Faghidian S, Smith D. A new analytical approach to reconstruct residual stresses due to turning process. International Journal of Mechanical and Mechatronics Engineering 2009;3(7):826–30.
[53] Farrahi G, Faghidian S, Smith D. An inverse method for reconstruction of the residual stress field in welded plates. J Press Vessel Technol 2010;132(6).
[54] Faghidian SA. A smoothed inverse eigenstrain method for reconstruction of the regularized residual fields. Int J Solids Struct 2014;51(25–26):4427–34.
[55] Chen MJ, Aquino W, Walsh TF, Reu PL, Johnson KL, Rouse JW, et al. A generalized stress inversion approach with application to residual stress estimation. J Appl Mech 2020;87(11).
[56] Slaughter WS. The linearized theory of elasticity. Springer Science & Business Media; 2012.
[57] Amrouche C, Ciarlet PG, Gratie L, Kesavan S. On the characterizations of matrix fields as linearized strain tensor fields. Journal de mathématiques pures et appliquées 2006;86(2):116–32.
[58] Wang Z, Stoica AD, Ma D, Beese AM. Diffraction and single-crystal elastic constants of inconel 625 at room and elevated temperatures determined by neutron diffraction. Materials Science and Engineering: A 2016;674:406–12.
[59] Gouge M, Michaleris P, Denlinger E, Irwin J. The finite element method for the thermo-mechanical modeling of additive manufacturing processes. In: Thermo-Mechanical Modeling of Additive Manufacturing. Elsevier; 2018. p. 19–38.
[60] Johnson GR, Cook WH. A constitutive model and data for metals subjected to large strains, high strain rates and high temperatures. In: Proceedings of the 7th International Symposium on Ballistics, vol. 21. The Netherlands; 1983. p. 541–7.
[61] Metals S, et al. Inconel alloy 718. Publication Number SMC-045 Special Metals Corporation 2007.
[62] Daw J, Rempe J, Knudson D. Thermal properties of structural materials used in LWR vessels. J Nucl Mater 2010;401(1–3):65–70.
[63] Hokka M, Gomon D, Shrot A, Leemet T, Bäker M, Kuokkala V-T. Dynamic behavior and high speed machining of ti-6246 and alloy 625 superalloys: experimental and modeling approaches. Exp Mech 2014;54(2):199–210.
[64] Ljustina G, Larsson R, Fagerström M. A FE based machining simulation methodology accounting for cast iron microstructure. Finite Elem Anal Des 2014;80:1–10.
[65] Buchkremer S, Klocke F, Lung D. Finite-element-analysis of the relationship between chip geometry and stress triaxiality distribution in the chip breakage location of metal cutting operations. Simul Modell Pract Theory 2015;55:10–26.
[66] Buchkremer S, Klocke F, Veselovac D. 3D FEM simulation of chip breakage in metal cutting. The International Journal of Advanced Manufacturing Technology 2016;82(1–4):645–61.
[67] Lu Y, Pan Z, Bocchini P, Garmestani H, Liang S. Grain size sensitive-MTS model for ti-6Al-4V machining force and residual stress prediction. The International Journal of Advanced Manufacturing Technology 2019;102(5–8):2173–81.
[68] Lotfi M, Jahanbakhsh M, Farid AA. Wear estimation of ceramic and coated carbide tools in turning of inconel 625: 3d FE analysis. Tribol Int 2016;99:107–16.
[69] Hooputra H, Gese H, Dell H, Werner H. A comprehensive failure model for crashworthiness simulation of aluminium extrusions. Int J Crashworthiness 2004;9(5):449–64.
[70] McClintock F.A.. A criterion for ductile fracture by the growth of holes1968;.
[71] Rice JR, Tracey DM. On the ductile enlargement of voids in triaxial stress fields. J Mech Phys Solids 1969;17(3):201–17.
[72] Hancock J, Mackenzie A. On the mechanisms of ductile failure in high-strength steels subjected to multi-axial stress-states. J Mech Phys Solids 1976;24(2–3):147–60.
[73] Hancock J, Brown D. On the role of strain and stress state in ductile failure. J Mech Phys Solids 1983;31(1):1–24.
[74] Bai Y, Wierzbicki T. A new model of metal plasticity and fracture with pressure and lode dependence. Int J Plast 2008;24(6):1071–96.
[75] Bao Y. Prediction of ductile crack formation in uncracked bodies. Massachusetts Institute of Technology; 2003.

[76] Bai Y, Teng X, Wierzbicki T. Study on the effect of the third stress invariant on ductile fracture. Report, Cambridge 2006.
[77] Algarni M, Bai Y, Choi Y. A study of inconel 718 dependency on stress triaxiality and lode angle in plastic deformation and ductile fracture. Eng Fract Mech 2015;147:140–57.
[78] Erice B, Gálvez F. A coupled elastoplastic-damage constitutive model with lode angle dependent failure criterion. Int J Solids Struct 2014;51(1):93–110.
[79] Matache G, Paraschiv A, Condruz MR. Tensile notch sensitivity of additively manufactured IN 625 superalloy. Materials (Basel) 2020;13(21):4859.
[80] Johnson GR, Cook WH. Fracture characteristics of three metals subjected to various strains, strain rates, temperatures and pressures. Eng Fract Mech 1985;21(1):31–48.
[81] Pantalé O, Bacaria J-L, Dalverny O, Rakotomalala R, Caperaa S. 2D and 3d numerical models of metal cutting with damage effects. Comput Methods Appl Mech Eng 2004;193(39–41):4383–99.
[82] Akram S, Jaffery SHI, Khan M, Fahad M, Mubashar A, Ali L. Numerical and experimental investigation of johnson-cook material models for aluminum (al 6061-T6) alloy using orthogonal machining approach. Advances in Mechanical Engineering 2018;10(9). 1687814018797794.
[83] Xie W, Yang F, Ding L, Scarpa F. Predictive models and experiments for high-velocity and high-temperature impacts in inconel-alloy panels. Materials & Design 2019;182:108032.
[84] Zhu Y, Engelhardt MD. Prediction of ductile fracture for metal alloys using a shear modified void growth model. Eng Fract Mech 2018;190:491–513.
[85] Schulz H, Moriwaki T. High-speed machining. CIRP Ann 1992;41(2):637–43.
[86] Machining nickel alloys. https://nickelinstitute.org/media/1719/machiningnickelalloys_11008_.pdf; N/A. Accessed: 2021-01-24.
[87] Renz A, Khader I, Kailer A. Tribochemical wear of cutting-tool ceramics in sliding contact against a nickel-base alloy. J Eur Ceram Soc 2016;36(3):705–17.
[88] Zubelewicz A. Century-long taylor-quinney interpretation of plasticity-induced heating reexamined. Sci Rep 2019;9(1):1–7.
[89] Wimpory RC, Hofmann M, Akrivos V, Smith MC, Pirling T, Ohms C. Precise measurement of steep residual strain gradients using neutron diffraction in strongly absorbing materials with chemical compositional gradients. Mater Perform Charact 2018;7(4):488–503.
[90] Goudar D, Hossain S, Truman C, Smith D. Uncertainty in residual stress measurements. In: ASME Pressure Vessels and Piping Conference, vol. 48296; 2008. p. 383–90.